Comparison of Randomly Undersampled Magnetic Resonance Imaging Reconstruction Methods

Xuetong Zhou, Qingyue Wei

Abstract—Compressed sensing is widely used in magnetic resonance imaging for it allows reduced scan time by sampling fewer data points in k-space. In this project, we mainly focus on the reconstruction of randomly undersampled images. ADMM with TV priors and Convolutional Recurrent Neural Network (CRNN) are investigated and compared with one of the conventional reconstruction methods – $l1$ wavelet regularized reconstruction. Three datasets are adopted to evaluate our methods including 1) Cardiac MR image dataset, 2) MRNet dataset, and 3) Brain tumor dataset. All the methods could effectively improve PSNR and remove artifacts. CRNN outperforms the ADMM based methods under all tested conditions. Compared with TV priors, $l1$ wavelet shows the best performance in improving PSNR but worst in artifact reduction.

Index Terms—MRI Reconstruction, Compressed Sensing, ADMM, $l1$ Wavelet, Total Variation, Convolutional Neural Network

1 Introduction

MAGNETIC resonance imaging is a noninvasive imaging modality with excellent soft tissue contrast. However, one of the main drawbacks of MRI is the long scan time needed to localize the MR signal to generate an image. Fast imaging is also limited by factors of hardware (gradient amplitude and slew rate), and physiological constraints, (nerve stimulation and patient discomfort). As time constrains the use of MRI in high-resolution imaging or dynamic imaging, compressed sensing is widely used to reduce the scan time.

In MRI, different from the natural images, sampled data points are stored in k-space, which is the frequency domain in MRI. Images are acquired by taking 2D Fourier transform to k-space data. When fewer data points are sampled in the k-space, the Nyquist criterion is violated thus leading to severe artifacts and a decrease in spatial resolution. Examples of undersampled MRI images are presented in Fig. 1. The uniformly undersampling pattern in k-space, for example, sampling evenly spaced rows, mainly results in aliasing artifacts, which can be resolved by many proposed methods exploiting the redundancy in k-space. Randomly undersampling pattern, however, leads to incoherent artifacts that become difficult to resolve. Reconstruction of a high-quality image from undersampled k-space data is important not only for clinical diagnosis but also for automatic processing.

In this project, we aim to focus on the random undersampling pattern, and use methods that we learned in class, such as ADMM with image priors and convolutional neural network, to mitigate the incoherent artifacts. The methods are evaluated with different undersampling rates and compared with one conventional MRI compressed sensing reconstruction technique – $l1$ wavelet regularized reconstruction [1]. Code is available at https://github.com/aijinrjinr/MRI_Reconstruction.

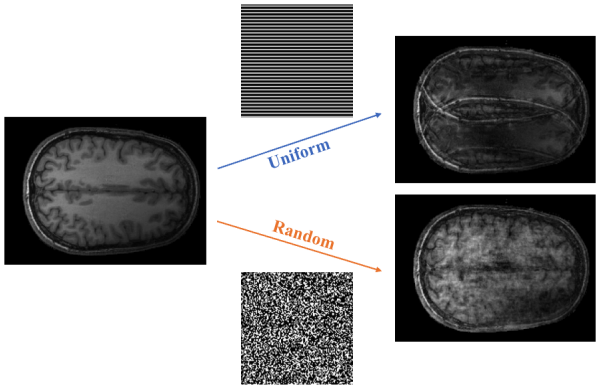

Fig. 1. Example of undersampling patterns and resultant images

2 Related Work

2.1 MR based methods

Currently, there are two major methods that can be used for the reconstruction of randomly undersampled MRI images, CG SENSE [2] and SPIRiT [3]. CG SENSE is a highly efficient reconstruction method proposed by Pruessmann *et al.* [2]. The forward model can be written as

$$F = Em \tag{1}$$

where m is the vectorized reconstructed image, F is the vectorized sampled data in k-space, E is the encoding matrix including terms of coil sensitivity and spatial encoding. Artifact reduced image is acquired by solving m

- *Xuetong Zhou is with the Department of Bioengineering, Stanford University.*
  E-mail: xuetongz@stanford.edu
- *Qingyue Wei is with Department of Electrical Engineering, Stanford University. E-mail: qywei@stanford.edu*

using conjugate gradient descent. One disadvantage of this method is that it requires accurate coil sensitivity maps [4].

SPIRiT, which is an iterative method proposed by Lustig *et al.* [3]. It recovers missing data points in k-space by exploiting correlations between neighboring k-space points. Within each iteration, weights of neighboring data points are estimated using calibration dataset. Missing data points are filled by convolving the weighting kernel with k-space until stop criteria is met. One drawback of SPIRiT is that it is relatively computationally intensive for it requires iteratively estimating weighting kernels from the calibration data and convolving the kernels with the data. In addition, it needs a calibration dataset.

2.2 Deep learning based methods

With the rapid development of Artificial Intelligence, deep learning based methods are now widely used for solving inverse and compressed sensing problems. Current popular methods could be divided into two groups. The first group mainly focuses on applying the unrolling method in a deep learning model. For example, Hammernik *et al.* [5] proposed a variational network that could combine the deep-learning method with a variational model. ADMM-Net [6] embedded the Alternating Direction Method of Multipliers (ADMM) algorithm into a deep-learning model for MR images reconstruction problems. And Adler *et al.* [7] utilized the prior information related to inverse problems in a deep-learning based method. The second group uses end-to-end deep learning methods. Schlemper *et al.* [8] built a deep cascade network that could effectively simulate the iterative reconstruction process for 2D Cartesian undersampling MR images. MICCAN [9] was constructed based on U-Net [10] and could pay more attention to high-frequency information by applying a long skip connection. And Wang *et al.* [11] proposed a parallel convolution neural network for MRI reconstruction and could take advantage of the correlation between the real and imaginary parts of MRI.

3 Proposed Method

3.1 Problem Formulation

Given an undersampled k-space data y, our goal is to reconstruct the artifact reduced images x. The optimization objective is

$$\arg\min_x \frac{1}{2}||Ax - y||_2^2 + \lambda||Fx||_1, \tag{2}$$

where A is the operator that represents taking 2D Fourier transform of the image and undersampling in k-space, F represents the operator of the image prior, λ represents the relative weight between the data fidelity and the regularization term.

3.2 $l1$ wavelet

Compressed sensing theory suggests that accurate reconstruction can be achieved using the knowledge that the image is sparse in some transform domain [12]. The reconstruction can be done by solving the nonlinear constrained optimization problem:

$$\begin{aligned} minimize \quad & ||\Psi m||_1 \\ s.t. \quad & ||\mathcal{F}_u m - y||_2 < \epsilon \end{aligned} \tag{3}$$

where Ψ is the linear operator that transforms the image to a sparse representation (*e.g.*, discrete cosine transform (DCT) and wavelet transform), m is the vectorized reconstructed image, $\mathcal{F}_u$ presented the operations including 2D Fourier transform and undersampling in k-space, y denotes the acquired undersampled k-space data [1]. Thus, the l1 norm of Ψm is used as a prior to promote sparsity of the data. The Daubechies-4 wavelet transform is used for the sparse operation.

3.3 Total Variation (TV)

Total variation exploits the fact that natural images are constituted by large regions of constant and sharp transitions between objects. TV promotes sparse gradient of the solution using the l1 norm of the image gradients [13]. Though it is firstly proposed for image denoising, TV has been found to be very useful in many inverse problems in image processing, for example, deblurring and restoration [14]. Anisotropic and isotropic TVs are investigated in this project:

$$TV_a(x) = \sum_{i=1}^{N} \sqrt{(D_x x)_i^2} + \sqrt{(D_y x)_i^2}, \tag{4}$$

$$TV_i(x) = \sum_{i=1}^{N} \sqrt{(D_x x)_i^2 + (D_y x)_i^2}, \tag{5}$$

3.4 ADMM

Alternating Direction Methods of Multipliers (ADMM) is used in this project to solve the optimization objective shown in Eq. 2. ADMM is an iterative approach to solve convex optimization problems by splitting the data consistency term and the regularization term in the objective function and solving them in an alternating manner [15].

The update equations are as follows:

$$x^{k+1} := (A^T A + \rho F^T F)^{-1}(A^T b + \rho F^T (z^k - u^k)), \tag{6}$$

$$z^{k+1} := S_{\lambda/\rho}(Fx^{k+1} + u^k), \tag{7}$$

$$u^{k+1} := u^k + Fx^{k+1} - z^{k+1}, \tag{8}$$

where F is the operator of the image prior which, in this project, refers to taking wavelet transform or computing the finite differences. Conjuagte gradient solver is used for x-update. Element-wise soft thresholding operator is used as the proximal operator for both $l1$ and TV priors.

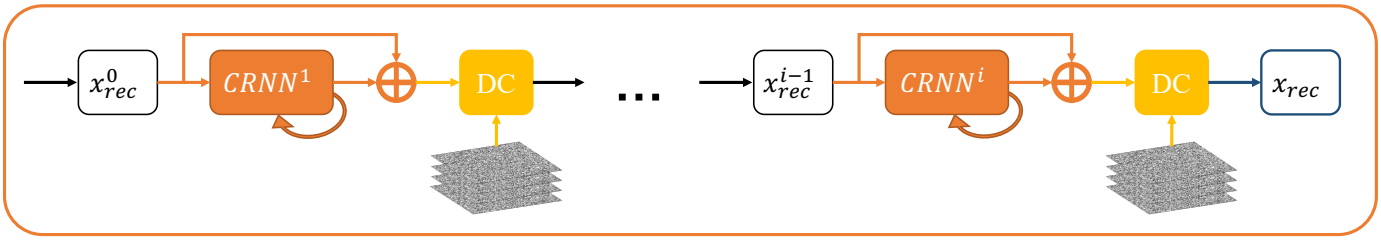

Fig. 2. Network structure for CRNN.

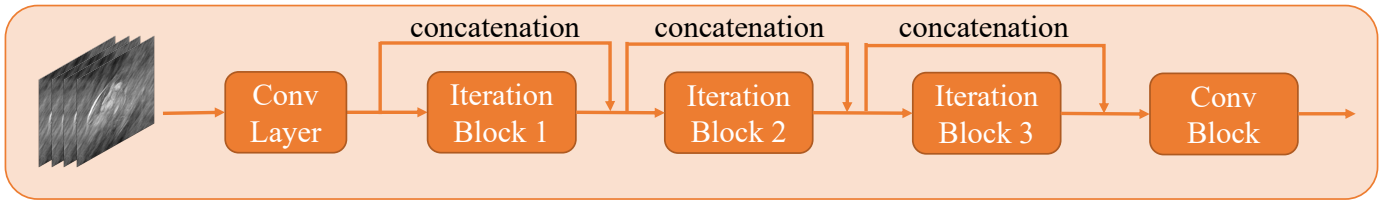

Fig. 3. Structure for CRNN Block.

3.5 CRNN

As for deep learning based model, following the idea of [16], we adopted a convolutional recurrent neural network (CRNN) architecture for MRI reconstruction. Unlike the unrolling methods (*e.g.*, ADMM-Net [6]), CRNN is an end-to-end network. It employs several recurrent blocks to simulate the iterative process of reconstruction. The whole reconstruction could be written as

$$\widetilde{x_i} = F_N(F_{N-1}(\dots(F_1(x_i, m_i; \theta_1)\dots); \theta_{N-1}); \theta_N), \quad (9)$$

where x_i is the i^{th} undersampling input, m_i is the relevant undersampling mask. $\widetilde{x_i}$ is corresponding reconstructed image. $F_j(\cdot)$ is the j^{th} simulated recurrent block and θ_j is corresponding parameters where $j = 1, 2, \dots, N$. N is the total simulated recurrent block number.

As shown in Fig. 2, for each recurrent block $F_j(\cdot)$, it consists of three components:

- 1) CRNN Block
- 2) Residual Connection
- 3) Data Consistency (DC) Layer

1) CRNN Block. As shown in Fig. 3, the CRNN Block is composed by a convolution layer, three cascade iteration blocks, and one convolutional block. To start with, the convolution layer is first applied to expand the channel dimension of input x_i. Then follows by three iteration blocks. Each iteration block is a cascade dense convolutional layer composed by [Batch normalization [17], 2 $\times$ (ReLU [18], convolution-layer)]. Denote the input and output of the s^{th} iteration block as $H_{in}^{s_j}, H_{out}^{s_j}$ where $s = 1, 2, 3$. The input of the $(s+1)_j^{th}$ iteration block is the concatenation of $H_{in}^{s_j}$ and $H_{out}^{s_j}$ along the channel dimension, denoted as $[H_{in}^{s_j}; H_{out}^{s_j}]$. And the final output is $[H_{in}^{3_j}; H_{out}^{3_j}]$. By concatenating the input and output of each cascade layer, the hidden information from different iteration steps could be analyzed at the same time and thus, could obtain useful feature from previous steps. Moreover, using cascade layers with multiple convolutional operators could help the network extract more complicated and abstract information. Specifically, here we adopt dilated convolutional operator in each cascade layer which could help expand the receptive field without losing information and the output could then contain a large range of information. And the number of input and output channels of these three cascade dense convolutional layers are (16, 16), (32, 16), (48, 16) respectively. As for the convolutional block, it includes 2$\times$[Batch normalization, ReLU, convolution layer].

2) Residual Connection. The output of the Residual Connection is

$$Out_i^{res} = \widetilde{x}_i^{j-1} + Out_i^{conv}, \quad (10)$$

where $\widetilde{x}_i^{j-1}$ is the input of $F_j(\cdot)$ and also the output of $F_{j-1}(\cdot)$ and $+$ indicates the pixel-wise addition. And Out_i^{conv} is the output of the last convolution layer in the Convolutional Block. With such residual operation, the reconstruction result from previous recurrent block could be taken into consideration simultaneously. Meanwhile, as the recurrent block number increases, residual connection could help prevent the degradation problem in the Deep Neural Networks [19] and alleviate the vanishing gradient problem as well.

3) Data Consistency (DC) Layer. To enforce the data fidelity between the reconstructed image $\widetilde{x}_i^j$ and the original undersampling image x_i, for each iteration block, a data consistency is applied to make sure the value of $\widetilde{x}_i^j$ in k-space at the sampled pixel is the same as it of x_i in k-space. Specifically,

$$\widetilde{x}_i^j = f^{-1}(f(Out_i^{res}) + (-f(Out_i^{res}) + k_i) \circ m_i), \quad (11)$$

where f means fast Fourier transform, f^{-1} is the inverse fast Fourier transform and k_i is the k-space undersampled input, m_i is the relevant undersampling mask. $\circ$ indicates the Hadamard product.

Loss. During training, at each step, given a batch of input $S = \{(x_i, y_i, m_i)\}_{i=1}^{b}$ where b is the batch size and y_i is the ground-truth image. We use the pixel-wise mean squared error (MSE) as the objective function where

$$\mathcal{L}(\Theta) = \frac{1}{b} \sum_{\substack{(x_i, y_i, \\ k_i, m_i) \in S}} ||\widetilde{x_i} - y_i||_2^2, \quad (12)$$

TABLE 1
Parameters used in ADMM

dataset	ρ	λ
Cardiac $l1$ wavelet	1e-2	4e-3
Cardiac TVa	3e-2	3e-3
Cardiac Tvi	3e-2	4.5e-3
Knee $l1$ wavelet	1e-2	4e-3
Knee TVa	3e-2	9e-3
Knee TVi	3e-2	1.2e-2
Brain $l1$ wavelet	1e-2	4e-3
Brain TVa	3e-2	3e-3
Brain TVi	3e-2	4.5e-3

TABLE 2
Average PSNR/SSIM from CRNN on different datasets in validation set

dataset	ratio	PSNR(dB)	SSIM
Cardiac	0.4	37.26	0.9536
Cardiac	0.6	45.26	0.9878
Cardiac	0.8	61.15	0.9996
Knee	0.4	32.12	0.9516
Knee	0.6	39.99	0.9870
Knee	0.8	51.04	0.9985
Brain	0.4	34.83	0.9019
Brain	0.6	41.39	0.9636
Brain	0.8	46.00	0.9843

where Θ is all the parameters of CRNN.

4 Experimental Results

Dataset and Evaluation Metric. We evaluate our methods on three different datasets including 1) Cardiac MR image dataset [20], 2) MRNet dataset [21], and 3) Brain tumor dataset [22]. Since our methods all deal with 2D data, for 3D image data, we use its 2D slices as inputs.

- **Cardiac MR image dataset** is a short-axis cardiac datasets which consists of 33 patients. Here we include 30 patients as the training dataset and the other 3 as the evaluation dataset. Following [16], the total selected slice number of training dataset is 3000, and 300 for validation. And inputs are padded with zero to the size of 256 $\times$ 256.
- **MRNet dataset** contains three different views (coronal, sagittal and axial) of knees MR images for each patient. Here we only include data in the coronal view. To save training time, we randomly pick 100 patients (1478 slices in total) out of 1130 from its training split as our training dataset and 10 patients (145 slices in total) out of 120 from its validation split as our validation dataset. And the original size of each slice is 256 $\times$ 256.
- **Brain tumor dataset** is composed by 3064 T1-weighted contrast-enhanced images in axial view. For better reconstruction, we only include 106 images with high-quality as our dataset. Among them, 94 images are used as the training dataset and 12 images as the validation dataset. Size of each image is 512 $\times$ 512. Under such setting, we also want to explore the ability of CRNN to deal with small dataset.

Two metrics, including Peak Signal to Noise Ratio (PSNR) and Structural Similarity (SSIM) are applied for quantifying reconstruction performance of CRNN. And PSNR is also used for evaluating the results of ADMM based methods.

4.1 Experiments details

For ADMM based experiments, three testing MR images, including one knee image, one cardiac image and one brain image, are retrospectively undersampled by randomly generated masks with the sampling rates of 80%, 60% and 40%.

For the ADMM experiments, the optimal convergence parameter ρ and the regularization weight λ are found empirically and used in generating the reconstructed images. The parameters for each experiment are presented in Table 1.

All experiments related with CRNN are implemented in PyTorch. Input images are resized to 256 $\times$ 256 for all experiments. We train all models with a batch size of 10 for 1000 epochs with 0.0001 as the learning rate. We apply Adam optimizer with weight decay at 1e-7. Besides those three testing images, for CRNN, we also evaluate its performance over the whole validation sets under three different undersampling rates mentioned above respectively.

4.2 Results

Comparison among all methods. Comparison of experiment results of three selected test images from corresponding validation sets are presented in Fig. 3-5. Their corresponding PSNR are listed in Table 3-5. All the methods can effectively reduce the undersampling artifacts and improve PSNR of all three test images.

Images reconstructed by CRNN show the highest PSNR values and restoration of details. Its superiority is most obvious on images with low undersampling rate of 40% and images with most fine details that are difficult to be reconstructed (*e.g.*, knee images). However, there are still incoherent artifacts left in the 40% sampled brain image.

Among the three image priors tested, $l1$ wavelet shows the greatest improvements of the PSNR values on the cardiac and brain images, while anisotropic TV produces highest PSNR values on knee images. However, by comparing the reconstructed images, $l1$ wavelet obviously has worst artifact reduction effect. Disturbing incoherent artifacts still exist on 40% sampled brain and knee images. Two TV priors show comparable PSNR improvement and artifact reduction. Both of them can restore a majority of detailed features even on images sampled with 40% data points in k-space. However, they produce another undesired effect, change of image contrast, which is obvious on 40% sampled brain and knee images.

Internal Comparison for CRNN. As shown in Table 2, CRNN achieve high PSNR and SSIM under all selected undersampling rates among these three datasets. Highest PSNR results in 61.15 dB when undersampling rate is 80% in Cardiac MR image dataset. And while the undersampling

TABLE 3
PSNR results for each method on the chosen cardiac image

ratio	Zero filling	$l1$ wavelet	TVa	TVi	CRNN
0.4	15.6	**25.9**	24.4	24.9	**37.4**
0.6	18.8	**30.5**	26.0	26.6	**44.2**
0.8	23.5	**38.9**	35.3	34.7	**62.9**

TABLE 4
PSNR results for each method on the chosen brain image

ratio	Zero filling	$l1$ wavelet	TVa	TVi	CRNN
0.4	15.5	**24.4**	23.7	23.8	**33.3**
0.6	18.6	**32.3**	30.0	29.9	**40.4**
0.8	24.2	41.3	**42.5**	42.1	**46.3**

TABLE 5
PSNR results for each method on the chosen knee image

ratio	Zero filling	$l1$ wavelet	TVa	TVi	CRNN
0.4	13.8	16.9	**21.0**	20.7	**31.4**
0.6	15.9	20.6	**21.1**	20.9	**39.0**
0.8	19.9	24.7	**32.1**	30.8	**49.7**

rate increases, PSNR also shows significant growth, especially for the Cardiac dataset.

5 Discussion

5.1 Comparison of image priors

One interesting result we find is that, compared to TV priors, $l1$ wavelet produces images with highest PSNRs but worst artifact reduction. In [1], $l1$ wavelet is proved to be more robust with variable density undersampling pattern in k-space, which is to have a higher sampling density near the center of k-space and a lower sampling density in the periphery of k-space. It is because the coarse-scale image components, which correspond to low-frequency region near the center of k-space, should be less sparse then fine-scale components, which correspond to high frequency in the periphery of k-space [1]. With the uniform density undersampling scheme that is used in this project, the coarse-scale components are suppressed due to the lack of low-frequency data in the data consistency constraint. This can explain the reason why $l1$ wavelet fails to remove all the incoherent artifacts.

For the resultant images acquired using TV priors, noticeable contrast change is caused by minimizing the $l1$ norm of differences in the images. This is also the reason of relatively low PSNRs of TV produced images. Some modifications of TV have been proposed to mitigate this contrast change, including forward and backward diffusion (FBD) [23], shock filters [24] [25]. A future work of this project would be using a modified TV prior to preserve image contrast without sacrificing artifact reduction effect.

5.2 Use of deep learning

For the CNN based method, although it outperforms ADMM based methods under all undersampling rates in three datasets, it requires much more data to train a good-performing model while ADMM based methods could deal with only a single image. Moreover, its performance also relies on the amount of data. As shown in Table 2, it's obvious that for the brain dataset which contains far less data, there is less increase in PSNR while having more sampled data points compared to the other two datasets. And in Table 4, PSNRs are very close between ADMM + anisotropic TV with CRNN when undersampling rate is 80%. Even though there is not a such big gap among different undersampling rates in brain dataset, CRNN still shows a quite robust performance considering we only train it with nearly 100 images. Besides the data limitation, CRNN can not handle different datasets or different undersampling rates using only one specific model. For each rate in every dataset, we need to separately train its corresponding model. Therefore, for future work, we believe a more general and robust CNN based model needs to be constructed (*e.g.*, combining with mode advanced modules) so that it is not sensitive to the type of data (*e.g.*, body parts) or the undersampling rates.

5.3 Constraints of this project

One limitation of this project is that all training and testing images used are fully sampled, coil combined images from online open dataset. However, in real MRI, data collection is performed using several receive coils. With each of the coils covering a small portion of the field of view (FOV), image with a full FOV can be acquired by taking root sum of square of all coil images. Multi-channel MRI is widely used for it can extend the FOV and retain a high signal to noise ratio (SNR). There is also a variety of approaches being proposed that exploit the coil domain redundancy on uniformly undersampled image reconstruction. A good review to these approaches can be found in [26].

A future direction of this project is to test all the methods with multi-channel raw MRI data. Reconstruction can either be done by adding a coil sensitivity operation in linear operator A of Eq. 2 or reconstruct coil images separately and combined in the last step. Both of these two ways, we assume, should be able to improve the reconstruction result and provide leeway for further reduction of the undersampling rate.

6 Conclusion

In this project, we have compared two methods for the reconstruction of randomly undersampled images which includes 1) ADMM based methods, and 2) a CNN based method. For ADMM based methods, we have implemented it with different priors including TV priors and $l1$ wavelet. For the CNN based method, we have applied CRNN. All methods are able to effectively improve PSNR and remove artifacts. Among ADMM methods, $l1$ wavelet outperforms the others but also shows weakness in artifact reduction. Among all conducted experiments, CRNN has shown the highest PSNR under different undersampled rates for all included datasets.

Acknowledgments

We would like to thank Qin *at al.* for providing the code for CRNN, Andreopoulos *at al.* for offering the public Cardiac

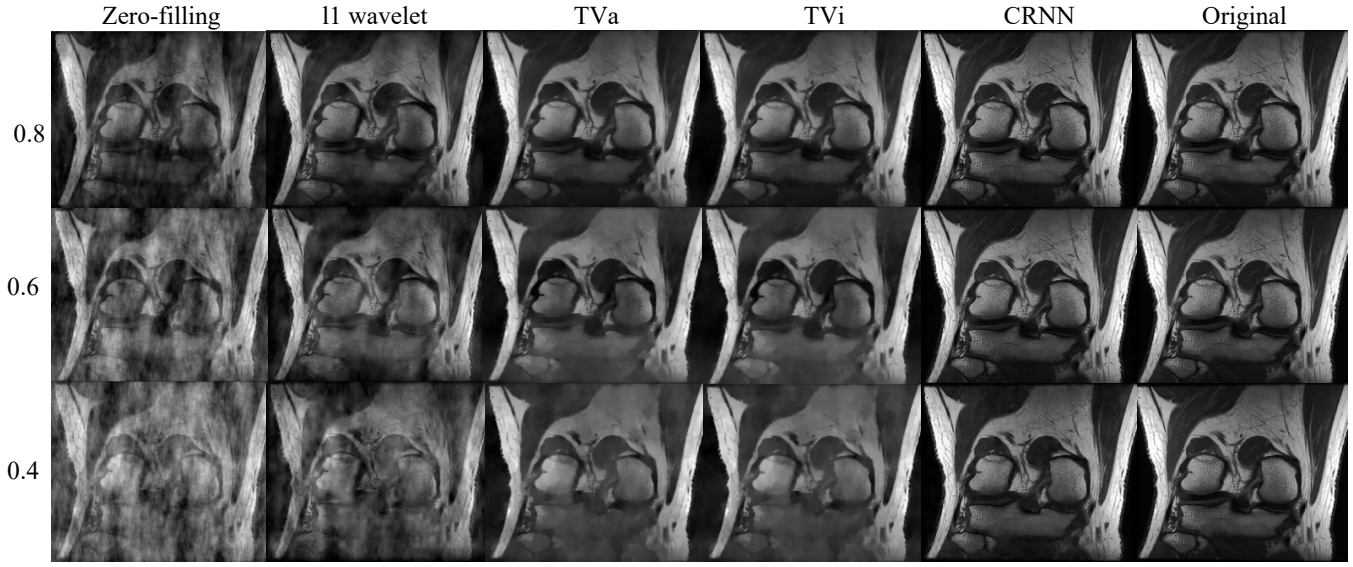

Fig. 4. Reconstructed knee MR images based on different methods.

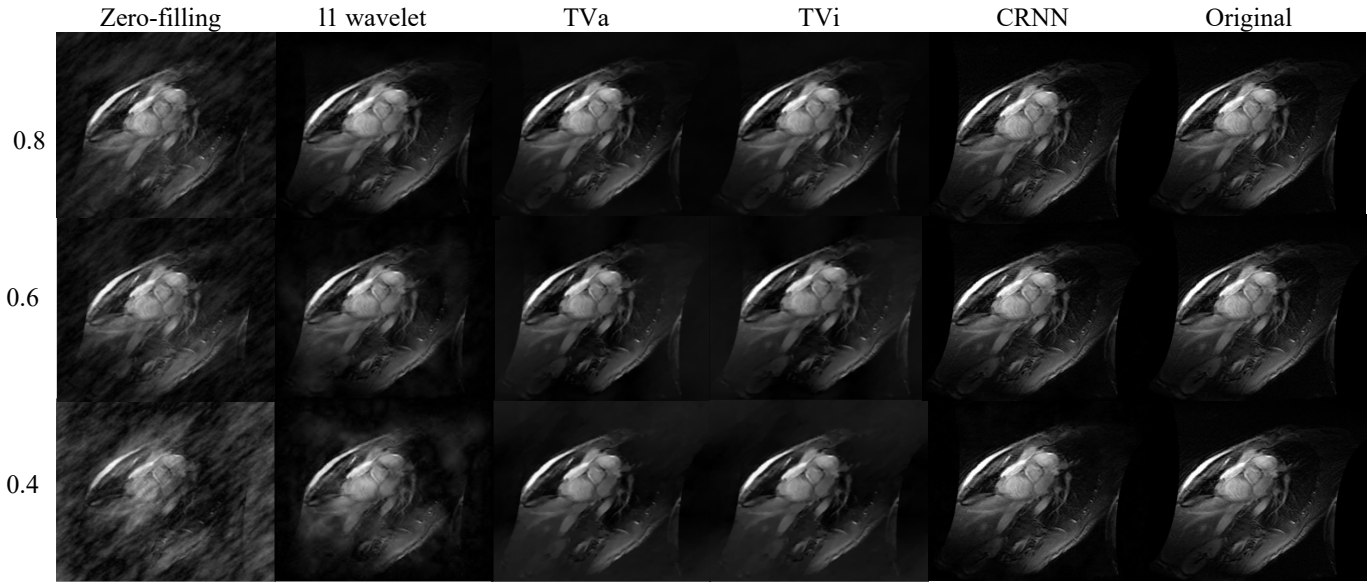

Fig. 5. Reconstructed cardiac MR images based on different methods.

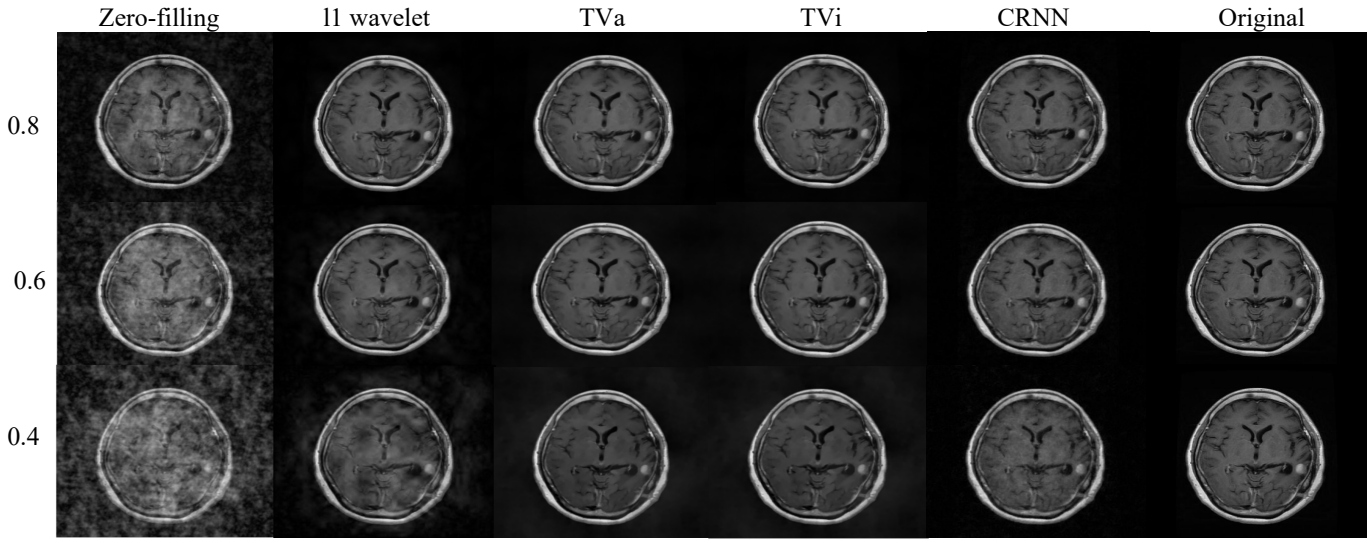

Fig. 6. Reconstructed brain MR images based on different methods.

MR image dataset, Bien *at al.* for MRNet dataset and Cheng *at al.* for providing the public Brain tumor dataset. We would also like to thank for all the help our mentor Mark Nishimura has given to us in this project, and Professor Gordon Wetzstein and Dr. David B. Lindell for offering such a wonderful class.

REFERENCES

[1] M. Lustig, D. Donoho, and J. M. Pauly, "Sparse mri: The application of compressed sensing for rapid mr imaging," *Magnetic Resonance in Medicine: An Official Journal of the International Society for Magnetic Resonance in Medicine*, vol. 58, no. 6, pp. 1182–1195, 2007.

[2] K. P. Pruessmann, M. Weiger, P. Börnert, and P. Boesiger, "Advances in sensitivity encoding with arbitrary k-space trajectories," *Magnetic Resonance in Medicine: An Official Journal of the International Society for Magnetic Resonance in Medicine*, vol. 46, no. 4, pp. 638–651, 2001.

[3] M. Lustig and J. M. Pauly, "Spirit: iterative self-consistent parallel imaging reconstruction from arbitrary k-space," *Magnetic resonance in medicine*, vol. 64, no. 2, pp. 457–471, 2010.

[4] K. L. Wright, J. I. Hamilton, M. A. Griswold, V. Gulani, and N. Seiberlich, "Non-cartesian parallel imaging reconstruction," *Journal of Magnetic Resonance Imaging*, vol. 40, no. 5, pp. 1022–1040, 2014.

[5] K. Hammernik, T. Klatzer, E. Kobler, M. P. Recht, D. K. Sodickson, T. Pock, and F. Knoll, "Learning a variational network for reconstruction of accelerated mri data," *Magnetic resonance in medicine*, vol. 79, no. 6, pp. 3055–3071, 2018.

[6] J. Sun, H. Li, Z. Xu *et al.*, "Deep admm-net for compressive sensing mri," *Advances in neural information processing systems*, vol. 29, 2016.

[7] J. Adler and O. Öktem, "Solving ill-posed inverse problems using iterative deep neural networks," *Inverse Problems*, vol. 33, no. 12, p. 124007, 2017.

[8] J. Schlemper, J. Caballero, J. V. Hajnal, A. Price, and D. Rueckert, "A deep cascade of convolutional neural networks for mr image reconstruction," in *International conference on information processing in medical imaging*. Springer, 2017, pp. 647–658.

[9] Q. Huang, D. Yang, P. Wu, H. Qu, J. Yi, and D. Metaxas, "Mri reconstruction via cascaded channel-wise attention network," in *2019 IEEE 16th International Symposium on Biomedical Imaging (ISBI 2019)*. IEEE, 2019, pp. 1622–1626.

[10] O. Ronneberger, P. Fischer, and T. Brox, "U-net: Convolutional networks for biomedical image segmentation," in *International Conference on Medical image computing and computer-assisted intervention*. Springer, 2015, pp. 234–241.

[11] S. Wang, H. Cheng, L. Ying, T. Xiao, Z. Ke, H. Zheng, and D. Liang, "Deepcomplexmri: Exploiting deep residual network for fast parallel mr imaging with complex convolution," *Magnetic Resonance Imaging*, vol. 68, pp. 136–147, 2020.

[12] D. Taubman and M. Marcellin, *JPEG2000 image compression fundamentals, standards and practice: image compression fundamentals, standards and practice*. Springer Science & Business Media, 2012, vol. 642.

[13] L. I. Rudin, S. Osher, and E. Fatemi, "Nonlinear total variation based noise removal algorithms," *Physica D: nonlinear phenomena*, vol. 60, no. 1-4, pp. 259–268, 1992.

[14] V. Caselles, A. Chambolle, and M. Novaga, "Total variation in imaging." *Handbook of mathematical methods in imaging*, vol. 1, no. 2, p. 3, 2015.

[15] S. Boyd, N. Parikh, E. Chu, B. Peleato, J. Eckstein *et al.*, "Distributed optimization and statistical learning via the alternating direction method of multipliers," *Foundations and Trends® in Machine learning*, vol. 3, no. 1, pp. 1–122, 2011.

[16] C. Qin, J. Schlemper, J. Caballero, A. N. Price, J. V. Hajnal, and D. Rueckert, "Convolutional recurrent neural networks for dynamic mr image reconstruction," *IEEE transactions on medical imaging*, vol. 38, no. 1, pp. 280–290, 2018.

[17] S. Ioffe and C. Szegedy, "Batch normalization: Accelerating deep network training by reducing internal covariate shift," in *Proceedings of the 32nd International Conference on Machine Learning*, ser. Proceedings of Machine Learning Research, F. Bach and D. Blei, Eds., vol. 37. Lille, France: PMLR, 07–09 Jul 2015, pp. 448–456. [Online]. Available: https://proceedings.mlr.press/v37/ioffe15.html

[18] A. F. Agarap, "Deep learning using rectified linear units (relu)," *arXiv preprint arXiv:1803.08375*, 2018.

[19] W. Fang, Z. Yu, Y. Chen, T. Huang, T. Masquelier, and Y. Tian, "Deep residual learning in spiking neural networks," *Advances in Neural Information Processing Systems*, vol. 34, 2021.

[20] A. Andreopoulos and J. K. Tsotsos, "Efficient and generalizable statistical models of shape and appearance for analysis of cardiac mri," *Medical image analysis*, vol. 12, no. 3, pp. 335–357, 2008.

[21] N. Bien, P. Rajpurkar, R. L. Ball, J. Irvin, A. Park, E. Jones, M. Bereket, B. N. Patel, K. W. Yeom, K. Shpanskaya *et al.*, "Deep-learning-assisted diagnosis for knee magnetic resonance imaging: development and retrospective validation of mrnet," *PLoS medicine*, vol. 15, no. 11, p. e1002699, 2018.

[22] J. Cheng, "brain tumor dataset," Apr 2017. [Online]. Available: https://figshare.com/articles/dataset/brain_tumor_dataset/1512427/5

[23] G. Gilboa, N. Sochen, and Y. Y. Zeevi, "Forward-and-backward diffusion processes for adaptive image enhancement and denoising," *IEEE transactions on image processing*, vol. 11, no. 7, pp. 689–703, 2002.

[24] S. Osher and L. I. Rudin, "Feature-oriented image enhancement using shock filters," *SIAM Journal on numerical analysis*, vol. 27, no. 4, pp. 919–940, 1990.

[25] L. Alvarez and L. Mazorra, "Signal and image restoration using shock filters and anisotropic diffusion," *SIAM journal on numerical analysis*, vol. 31, no. 2, pp. 590–605, 1994.

[26] J. Hamilton, D. Franson, and N. Seiberlich, "Recent advances in parallel imaging for mri," *Progress in nuclear magnetic resonance spectroscopy*, vol. 101, pp. 71–95, 2017.